Resistivity and chargeability survey for tunnel investigation: a case study on toxic black shale in Norway

S. Bazin[1], A.K. Lysdahl[1], A. Viezzoli[2], T. Günther[3], H. Anschütz[1], J. Scheibz[1], A.A. Pfaffhuber[1], T. Radic[4], H. Fjermestad[5]

[1] sara.bazin@ngi.no Norwegian Geotechnical Institute, Sognsveien 72, 0855 Oslo, Norway

[2] Aarhus Geophysics, ApS. C.F. Møllers Allè 4, DK-8000 Aarhus C, Denmark

[3] Leibniz Institute for Applied Geophysics, Hannover, Germany

[4] Radic Research, Berlin, Germany

[5] Statens vegvesen Region øst, Postboks 1010, 2605 Lillehammer, Norway

Abstract

In the past few years, the focus on Alum shale hazards and the need for efficient mapping tools have increased in Norway. Alum shale is highly toxic and poses a substantial obstacle to infrastructure development such as tunnel projects. We present an evaluation of the ground-based electrical resistivity tomography (ERT), induced polarization (IP), and airborne electromagnetic (AEM) methods for mapping purposes using a recent case study. This

evaluation is done in combination with resistivity and chargeability laboratory measurements applied on drill cores. The aim of the geophysical survey was to improve the knowledge of Alum shale occurrence to assist a tunnel project in Gran, southeast Norway. Resistivity and chargeability models derived from an ERT/IP survey enabled us to map the presence of Alum shale during the tunnel investigation. The resistivity models point to geological layers that are in agreement with the rock types observed from early drillings together with subsequent geological logging during tunnelling. The time-domain chargeability models are imperfect but nonetheless reveal the presence of polarizable minerals. These are likely due to the high levels of sulphides contained in black shale. An AEM survey was flown close to the area of interest which enabled us to fly some sparse lines across the tunnel alignment as a piggyback survey. Although the AEM resolution is lower than ERT, the successful test flight lines illustrate the potential of AEM surveys for Alum shale mapping in Norway.

Keywords

Electrical resistivity tomography, IP, black shale

Running head

Ground-based, laboratory, and airborne investigations to map black shale from resistivity and chargeability.

Introduction

The Norwegian Road Authority is modernizing the highway Rv.4, located 80 km northwest of Oslo (Figure 1). Two parallel road tunnels, each 1700 m long, have been excavated to bypass the town of Gran. The rock overburden is between 15 m and 25 m. The blasting took place between November 2013 and May 2015 and roughly 335 000 m^3 of masses from 700 blasting units were driven out. The tunnel will open to traffic in summer 2017. We carried out a geophysical survey along the planned tunnel axis as blasting had just started. Exploratory drilling had already been conducted and a preliminary geological model was available. However, the complexity of the project required a supplementary study to gather continuous information between the boreholes and thus decrease the overall project risk in terms of finances and scheduling. The first objective of this study was to characterise the rock mass and its overburden using resistivity derived either from ground-surface ERT or AEM surveys.

Experience shows that ERT usually gives good results for tunnel investigations (Danielsen and Dahlin, 2009) and it is a time and cost effective method compared to other ground-based geophysical methods. Conversely, the use of AEM for tunnel pre-investigations is only starting for economic reasons and an increasing number of case studies shows that high-resolution AEM data is a valuable and cost-saving tool in construction projects (Pfaffhuber *et al.*, 2010, Okazaki *et al.*, 2011, Anschütz *et al*., 2017). The typical size of an AEM survey for such projects is on the order of 200 km flight lines which takes approximatively 2 - 3 days to fly. Both methods, ERT and AEM, can model the lateral and vertical resistivity distribution of the subsurface, ERT has often a better lateral resolution but more limited depth of investigation than AEM (e.g. Anschütz *et al.*, in review). The two methods are therefore complementary.

The second objective of this study was to determine the applicability of geophysics to identity the different shale types present in the tunnel. Some areas of the Norwegian capital Oslo and

its surroundings feature a toxic black shale type, Alum shale. Excavated Alum shale is classified as toxic waste and must be disposed accordingly (NGI, 2015). For this purpose, a special waste landfill needs to be established near the excavated site. Consequently, Alum shale occurrence is a massive cost for a tunnel project, and prior knowledge about its expected volume is crucial. The resistivity models were initially used to delineate the occurrence of the black shale along the tunnel axis. We observed that the black shale was chargeable enough to create IP signals in both the ground and airborne data. Laboratory measurements were then carried out at a later stage to help understand the different mechanisms involved in the IP signals observed in the field. The results of the different methods are first described, then compared and discussed. An evaluation of the different mapping methods is proposed.

Geological context

The Alum Shale Formation is a formation of black shale of Middle Cambrian to Lower Ordovician in age, found only in southern Scandinavia (Nielsen and Schovsbo, 2007). They were deposited in an alternation of reducing or oxidizing environmental conditions as dark, fine-grained sediments rich in organic material (NGU, 2009). These shale formations have a high content of carbon, with total carbon values (TOC) up to 16-17% (wt). In certain extreme TOC values up to 50% (wt) have been found. Alum shale is known to be environmentally harmful because of its high content of sulphides (> 15 g/kg) and heavy metals (60-200 mg/kg) (NGI, 2013). Alum shale is also a source of radon gas and ionizing radiation. Adding to its toxicity, Alum shale swells significantly when it encounters oxygen, leading to deformation and damage risk to infrastructure in the vicinity: the oxidation changes the shale minerals such that a significant swelling perpendicular to the shale plane occurs (2-3 times the original volume), which can cause differential uplift to nearby structures (NGI, 2015). Moreover, when exposed to air and water, the sulphides are oxidized and produce sulfuric acid, which may corrode metallic structures. Black shale formations in Norway are mainly

found in the Oslo rift which extends as far north as Hamar, about 130 km north of Oslo. They are found on a small but densely inhabited area (roughly one third of the Norwegian population lives in southeast Norway). These clay-rich shales are part of the Cambro-Silurian stratigraphy, which includes a wide variety of shales and limestones of different compositions. The different lithological black shales in the Oslo graben have been formed under different anaerobic conditions. Less oxygen present under sedimentation generally produced higher sulphide and heavy metal contents and larger grain sizes. The shale layers are named chronologically: Layer *1* designates the oldest, deepest layer and consists mainly of sandstones. Layers *2-3a* comprise the most harmful black shale, named Alum shale, usually in thick layers (up to 80 m). Alum shale is an argillaceous, often carbonaceous rock, containing iron sulphides (pyrite, pyrrhotite and marcasite) which, when decomposed, forms sulphuric acid that reacts with the aluminous and potassic materials of the rock to produce aluminium sulphates (AGI 1972). Layer *3bα* is called Hagaberg and is a green-gray shale, usually with a thickness of over 10 m. Layer *3bβ* is another black shale, called Galgeberg, with a thickness of over 15 m. Thereafter comes layer *3c*, typically a thin layer subdivided into limestones, called Huk, and limestone-rich shales. The last layer found in the Gran tunnel is *4aα*, called Elnes, a gray shale that may have black shale properties, and can occur in layers dozens of meter thick. The strata are tilted in the area and the Alum shale layer is exposed in the northern tunnel end. Nyland and Teigland (1974) measured uranium (U) concentration in many samples from Cambro-Silurian rocks of the Oslo rift and they reported that the Alum shale samples contained the highest U concentration (126 mg/kg), compared to an average of 29 mg/kg in the remaining samples.

Laboratory data

Resistivity measurements were carried out on cores drilled in the Gran tunnel. They correspond to the five rock types of the Cambro-Silurian stratigraphy. The samples were carefully sawn off and their final average dimensions were 38 mm in diameter and 31 mm in

length (Figure 2 right). Wang *et al.* (2009) have adapted a triaxial cell to measure resistivity in rock samples at in-situ conditions while minimizing the polarization effects with a two-electrode system (Figure 2 left). The modified triaxial cell was used at a confining pressure of 0.5 MPa and a varying effective vertical stress of 3-10 MPa. Both axial and radial resistivity were recorded. The maximum (perpendicular to the shale plane) and minimum (parallel to the shale plane) resistivity were estimated by rotating the conductivity tensor (Table 1).

	Elnes	Huk	Galgeberg	Hagaberg	Alum
Max. resistivity (Ωm)	84	540	0.54	240	0.13
Min. resistivity (Ωm)	44	43	0.25	110	0.025

Table 1: Laboratory resistivity measurements in core samples from the five rock types of the Cambro-Silurian stratigraphy. The laboratory set-up and the Alum shale sample are shown in Figure 2.

The two black shale types (Alum and Galgeberg) are highly conductive, $\rho < 1$ Ωm, the Alum shale being the most conductive. These extremely low values confirm the potential to use resistivity as a mapping tool for black shale. The gray shale Elnes, which may have some black shale properties, has a higher resistivity, whereas the Hagaberg and the limestone Huk have much higher values. The strong anisotropy, up to a factor of 10 for Huk limestone and Alum shale, is of particular interest. The former is explained by significant cracks visible in the sample, the latter is a result of the inherent sedimentation structure.

As explained in the introduction, the second objective of this study was to determine the applicability of geophysics to identity the different shale types of the Cambro-Silurian stratigraphy. The need to better understand the chargeability properties of Alum shale was raised while processing the ground-investigation data. Therefore, spectral IP (SIP) measurements were carried out on three core samples at a later stage using the "Chameleon" apparatus (Radic, 2014) to measure the complex resistivity ρ^* ($\rho^* = |\rho| e^{i\varphi}$ where φ is the phase shift between the injected current and the measured potential). These

samples were not taken in the Gran tunnel but from the same Alum shale layer of the Cambro-Silurian stratigraphy in the Oslo graben. Again, the samples were carefully sawn off and their final average dimensions were 45 mm in diameter and 96 mm in length. The SIP measurements were carried out with three different current densities (0.07 A/m^2, 0.7 A/m^2, and 7 A/m^2) but only the most representative one, at 0.07 A/m^2, is shown here. Figure 3 shows the resistivity spectra (amplitude |ρ| and phase φ) in three Alum shale samples (E1, E2, and E3). The measured impedance is a combination of several mechanisms. The most important of these for the investigated samples is the current flowing through metallic particles, which creates a frequency dependent conduction. This mechanism is usually referred to as interfacial polarization. We observe a decrease of the amplitude resistivity with increasing frequency (Figure 3 a) which is connected with a negative phase shift between the injected current and the measured voltage (Figure 3 b). The chargeability level can be estimated from the relative drop of resistivity from lowest to highest frequency by the formulation $m_o = (\rho_0 - \rho_{inf}) / \rho_0$. It ranges between 650 and 800 mV/V for the three samples over the entire spectrum (Figure 3 a). The three phase spectra in Figure 3 b seem to indicate that these Alum shale cores have different polarization performance over the studied frequency (1 mHz to 100 kHz) but they all show three phase peaks at the same frequencies (at 3 mHz, between 2 and 3 Hz and near 100 kHz). The phase decrease near 100 kHz should not be considered a characteristic peak. The measured peak amplitudes are between 1° and 19°. Normally IP effects over 1° phase are due to electronic conducting minerals, i.e. the iron sulphides present in these Alum shale cores. The peaks in the spectrum are interpreted as related to the diameters of electronic conducting minerals (e.g. Pelton *et al.*, 1978). The phase peak at 2-3 Hz corresponds with minerals' diameters of some mm while the phase peak at 3 mHz corresponds with minerals' diameters of some cm. A visual inspection does not show minerals as large as cm and thus the phase peak at 2-3 Hz can be a result of connected conducting minerals, forming large polarisable aggregates. Such aggregates are visible in the samples and have the shape of foliations. In general the

amplitude of the phase peak correlates with the mineral content of the sample (Pelton *et al.*, 1978; Revil *et al.*, 2017). A chemical analysis of the three samples reveals that the two samples (E2 and E3) that present a strong peak near 3 mHz contain the most iron sulphides and the highest U levels, and, are therefore the most harmful. This result highlights the heterogeneity that can be found in one single Alum shale layer. These rocks have probably been formed under more anaerobic conditions, yielding higher sulphide content and larger grain sizes (Lysdahl *et al.*, 2016). This result also suggests that the amplitude of the phase peak may be a good proxy for the toxicity level of the Alum shale.

Resistivity ground investigation

ERT measurements were carried out along the tunnel axis to map the occurrence of black shale motivated by prior laboratory tests indicating extremely low resistivity (< 1 Ωm, see above). The survey was performed with a 12-channel Terrameter LS recording unit (ABEM, 2010). The multiple gradient array was chosen for the acquisition protocol (Dahlin and Zhou, 2006) being the most efficient array for this multichannel instrument. Three ERT profiles with 3 m electrode spacing (profile lengths: G1 420 m, G2 582 m, and G3 519 m) were acquired along most of the tunnel alignment. The maximum depth of investigation was ~46 m with this acquisition geometry. Two additional ERT profiles (G4 and G5) were acquired in the central part of the tunnel alignment with 5 m electrode spacing to increase the depth of investigation to 70 m where the tunnel is the deepest (the depth of the tunnel roof at its deepest point is 44 m). All ERT data were inverted with the academic Boundless Electrical Resistivity Tomography (BERT/GIMLi) code (Günther *et al.*, 2006). Bazin *et al.* (2015) discuss the consistency between this inversion algorithm and the industry standard Res2Dinv program (Loke, 2010) together with the Århus University's ArhusInv algorithm (Auken *et al.*, 2005; 2014). Figure 4 Illustrates the three different stratigraphy models that exist for the tunnel project: pre-investigation geological mapping and borehole lithology were used to build a preliminary stratigraphic model, resistivity models were used to foresee possible deviation

from the preliminary stratigraphic model, finally, direct geological observation during the excavation were used as ground-truth to evaluate the resolution of the resistivity models. Only the three most representative of the five ERT profiles are presented here for the interpretation with the geology. The parallel profiles are consistent and corroborate our interpretation. 2D resistivity sections acquired during excavation (Figure 4 a) enabled us to map geological layers in agreement with the rock types expected in the geological model based on early drill logs (Figure 4 b). The folding of the resistive Huk limestone layer (its laboratory resistivity ranges from 43 to 540 Ωm, c.f. Table 1) is recovered by the resistivity models. The Hagaberg layer (ρ = 110-240 Ωm) is too thin to be resolved between the two conductive shale layers (Galgeberg with ρ = 0.25-54 Ωm and Alum with ρ = 0.025-0.13 Ωm). The presence of black shale is suggested by the very low resistivity (< 1 Ωm, dark blue in Figure 4 a) within the northern 2/5th of the tunnel. This was later confirmed by direct geological observation during the excavation; the final geological mapping is depicted in the tunnel outline (Figure 4 b). The preliminary stratigraphic model provided a general understanding of the expected geology but the direct geological observation revealed that the Huk layer thickness is variable and that all the layers are more folded than predicted.

Chargeability ground investigation

Time Domain IP (TDIP) was also measured during the ERT survey. Acquisition settings were kept equal for the different profiles: a square-wave voltage input with 1 s on- and off-time was applied and full-waveform data were recorded. This short time period was chosen due to the survey's primary focus on resistivity. For the same reason, non-polarizable electrodes were not used as they are fragile and not practical in hard ground conditions. Stainless steel electrodes were used for current transmission as well as potential measurements. The Terrameter measurement protocol is specially designed to minimize electrode charge-up by making sure electrodes are not used for measuring potentials immediately, or soon after, being used for transmitting current (Dahlin, 2000). Logarithmically spaced gates windows

were used for the IP acquisition during current time-off (50 % of the duty cycle). Figure 5 shows the raw field data as apparent resistivity and apparent chargeability sections along one representative profile, G3, with 3270 data points. The resistivity data are of generally good quality but the IP data appear erratic as we observe very negative and very positive apparent chargeability values next to each other. It is generally observed that field resistivity data acquisition is robust from a data quality point of view, whereas IP data acquisition is much more sensitive to noise contamination due to smaller signal levels in combination with shorter delays and integration times (Dahlin and Leroux, 2012). Apparent chargeability values above 200 mV/V as measured here, are usually considered unrealistic and affected by noise in near surface investigations, but are common in mineral exploration (*e.g.* Viezzoli and Kaminski, 2016). In this case, the occurrence of high absolute apparent chargeability values is stronger for the early gate (IP1 gate goes from 0.01 to 0.03 s) than for the later gate (IP9 goes from 0.75 to 0.99 s). The injected current varied between 83 to 503 mA, with the low current values being concentrated in the conductive areas (mostly towards the north). This would indicate that the IP data quality is expected to be lower due to smaller signal levels in the vicinity of Alum shale, which was the aim of the survey. Negative apparent chargeability values can occur as a consequence of the distribution of chargeable zones in the ground (Dahlin and Loke, 2015), they were therefore kept during the data processing. An inspection of the full-waveform voltage data measured along G3 indicates that some areas reveal good quality voltage data (Figure 6), which is the case for most of the shallow part of the profile. However a large part of the full-waveform voltage data reveal ambient noise most likely due to the nearby infrastructures (Figure 7). Such noise is frequent and Olsson *et al.* (2015) have improved the acquisition software and hardware to minimize this, but these developments were not available at the time of this survey. Some of the areas affected by ambient noise can still present the usual shape for the decay curves (Figure 7) even though the voltage measurements are erratic. This indicates that manual data editing is not possible based only on the shape of the decay curves. In addition to the anthropogenic noise the

voltage data might also be contaminated by EM coupling within the measuring cables and this noise most often affects the first gate. EM coupling noise can be important while using the multiple gradient array as the potential electrode pair is located inside the current electrode pair. Dahlin and Leroux (2012) have reduced this type of noise by using two separate multi-electrode cables for the potential and current dipoles. This was unfortunately not doable here with the limited time available for the survey and, again, because the resistivity measurements were the priority.

Some decay curves are so erratic that it was not possible to manually edit the raw data and keep enough decays to successfully invert for the Cole–Cole relaxation parameters with AarhusInv inversion algorithm (Fiandaca *et al.,* 2013). At the time of this research, AarhusInv was not able to invert such sparse data. In the meantime, a constant phase angle inversion was implemented. Instead of fitting the full shape of the decay curves, one can limit the IP inversion to the integral chargeability, which is the integration of the area beneath each decay curve. The magnitude of the integral chargeability can be computed by discrete integration at the 9 time gates with Res2DInv (Loke, 2010). The Res2Dinv resistivity and integral chargeability results are presented in Figure 8 ab, Figure 9 ab and Figure 10 ab for profiles G1, G4, and G3 respectively, going from S to N. As already discussed in Bazin *et al.* (2015), the resistivity models obtained with the two inversion algorithms, Res2inv (Figures 8-10 a) and Bert/GIMLi (Figures 8-10c) are quite similar. The earlier comparison of Bazin *et al.* (2016) plotted the inverted models obtained from the different algorithms with the same visualisation tool. Here, for simplification the two built-in visualisation tools are used but with the same range of values for the colour scales. The IP data fit is already very good (RMS = 2.3 %) at iteration 4 for G1, but only fair (RMS = 10.5 %) at iteration 5 for G3, and poor at iteration 5 for G4 (RMS = 13,6%) with Res2Dinv (Figures 8-10 b). As is typical for noisy IP data, the inverted chargeability appears spotty. The background chargeability level is low for most of G1 except in the northern end which presents a strong but small-scale anomaly. Indeed, the later geological mapping revealed the presence of Galgeberg black shale near

G1 northern end. The chargeability models along G4 and G3, are more variable than along G1. A quite contiguous feature is observed along G1 and G3 profiles in the first 15 m depth, which traces the sediment-bedrock interface. In addition, some strong blocky anomalies are seen along G3 and G4 within the bedrock but it is difficult to interpret them in terms of geology.

Alternatively, the spectral IP effect can be modelled by the BERT/GIMLi algorithm (Günther and Martin, 2016). Like other algorithms, it begins with a DC resistivity inversion prior to inversion of the IP data. Usually it works in the frequency domain, either for single frequencies or simultaneously for the whole frequency spectrum (Günther and Martin, 2016). However, this algorithm also includes an inversion for chargeability using an inversion approach based on the ideas of Oldenburg and Li (1994), and combining two different DC forward calculations. Data are the measured apparent chargeabilities for any time gate and inversion parameters are the subsurface chargeabilities (in mV/V), which are directly regularized by smoothness constraints and a logarithmic transformation. As a result, contiguous and thus more realistic IP models are obtained, compared to linearized inversion approaches. The BERT resistivity (Figures 8-10 c) and chargeability (Figures 8-10 d) models are presented for the three selected profiles. There is reasonable agreement between Res2DInv (Figures 8-10 b) and BERT chargeability models (Figures 8-10 d) while the BERT models appear less spotty thanks to the new regularization. The chargeability residuals obtained are reasonable, 11.5, 19.3, and 18.9 mV/V for G1, G3, and G4 respectively. This adds confidence to the interpretation of the ground-based chargeability models. Like for the Res2DInv RMS, these chargeability residuals reveal that the data are noisier towards the north with the presence of black shale. As for the Res2DInv models, a contiguous chargeability contrast traces the sediment-bedrock interface. This feature is in accordance with the preliminary geological model. In addition, some strong chargeability anomalies are observed within the bedrock: near x=340 m along G1, between x=200 and 400m along G4,

and along most of G3. These coincide with the conductive regions and observations of black shale.

AEM test survey

A small AEM test survey was carried out with the SkyTEM 304 time domain system (Sørensen and Auken, 2004) as part of a bigger survey (Lysdahl *et al.*, 2015). Raw data were processed using the Århus Workbench package (www.aarhusgeo.com) and inverted using a spatially constrained inversion (SCI, Viezzoli *et al.*, 2008). The AEM time gates range from 8.21 μs to 8.90 ms. Figure 11 shows a sample of the AEM data collected during two minutes of flights. The raw data quality suffers from the noisy background caused by the urban area. However, unlike for the ground-based IP data, the AEM data can be edited through careful inspection of the transients, carried out using available ancillary GIS information (*e.g.,* Auken *et al.*, 2009). Failure to do so can result in significant artifacts in the models (Viezzoli *et al.,* 2012). The data coverage is sparse because the helicopter could not fly above buildings. The penetration depth of the AEM method is in excess of 100 m in this area, more than twice that of the short ERT profiles. The nominal spacing between AEM sounding points were 30 m. The 1D-vertical resistivity models were projected along the Gran tunnel and are depicted in Figure 12 a. Although the resulting profile does not perfectly coincide with the ground investigation lines (cf. map in Figure 1), the AEM resistivity depth section agrees with those obtained with BERT (Figure 4 a) and the geological mapping (Figure 4 b). The very conductive black shale (Galgeberg and Alum shales, dark blue on the resistivity colour scale) is easily identified in the AEM resistivity section: the small-scale undulations are not recovered but the black shale layer deepens towards the south.

The spatial distribution of the resistivity is presented in map views at three different elevations (Figure 13). The very high conductivity ($\rho < 1$ Ωm, dark blue on the resistivity colour scale) is in agreement with the presence of Alum shale near the northern end of the tunnel. The distribution of radioactive nuclides (Th, U, K) was mapped with a light gamma

spectrometer mounted on the helicopter. It measured the intensity of gamma radiation emitted from the ground, from the isotopes 232 thorium, uranium 238 and 40 potassium. The U distribution is also depicted in Figure 13 and it presents a strong anti-correlation with the resistivity distribution at the highest of the three elevation slices (210-220 m). As expected, the uranium level is the strongest where the Alum shale layer is shallowest near the northern end of the tunnel. This method therefore can be used for efficient large-scale investigation of Alum shale, however Heincke et al. (2008) have noticed that clayey marine sediment covers can strongly attenuate gamma radiation. It might therefore not be as reliable as resistivity/IP surveying.

The presence of strong IP signals in the laboratory and ground data suggested the possibility of modelling IP from the SkyTEM data. It has long been known that chargeability can affect time domain AEM systems (*e.g.,* Smith and Klein, 1999). A better understanding and monitoring on AEM systems' responses, associated with recent developments in inversion codes (*e.g.,* Fiandaca *et al.*, 2013) has renewed interest in this topic and its applicability (Kratzer and Macnae 2012, Kaminsky and Viezzoli, 2017). The AEM data need proper pre-processing; then a dispersive resistivity formulation takes place of the standard non dispersive resistivity. Negative raw TDEM data are a sure indication of IP effects, for a concentric TDEM system. Negatives develop more easily in the presence of resistive bedrock, which is not present in this area. Lack of negatives, however, does not exclude the presence of an IP component, which could be associated with an increase of signal at the early times and/or a slightly faster decay at later times (*e.g.,* Smith and West, 1989). IP modelling was therefore attempted, using the Cole-Cole model. On average, the data misfit decreased by approximately 15%. The resistivity changed only marginally. The sensitivity on the Cole-Cole models is generally low, with a depth of investigation for chargeability on the order of 50 m (Christiansen and Auken, 2012). However, the chargeability distribution inverted from the AEM dataset (Figure 12 b) shows a strong correlation with the presence of

Alum shale just below or in the tunnel, from distance x = 400 to 600 m and an even stronger correlation towards the northern end of the tunnel from distance x = 1250 to 1400 m (the purple colour Figure 12 b indicates chargeability levels > 200 mV/V).

Discussion

ERT surveys are widely used for site investigations during the design stage of construction projects. IP surveys however are hardly ever used. In this study, the benefit of the IP measurements in conjunction with the resistivity measurements was examined. Although the ground-based IP data are very noisy and the TDIP setup was not optimal for a chargeability investigation, the ground-based IP models (Figures 8-10 d) clearly indicate a strong polarization where the black shale was mapped by geologists (direct observation in the tunnel and cores). This black shale could have been imaged by the ground-based resistivity survey alone, but they were confirmed by the TDIP survey with no extra cost and therefore decreased the overall project risk. Further data pre-processing should be considered to improve TDIP data quality in the future. The new inversion approach in the BERT/GIMLi algorithm substantially improved the quality of the chargeability models compared to the linearized inversion.

As already mentioned by Wennermark *et al.* (2015), the two different types of IP acquisition (time-domain in the field and frequency-domain in the laboratory) are qualitatively connected, but it is difficult to proceed to a quantitative comparison. Exploiting the full decay spectrum of the ground-based IP data may allow such comparison in the future. The TDIP field experiment uses a transmitter frequency of ~0.2 Hz. At this frequency all three Alum shale samples show a significant phase lag (6° to 8°) and a chargeability level of ~200 mV/V over the Terrameter bandwidth range. There is thus good agreement between the ground-based TDIP and the SIP laboratory test. It would be interesting to address whether different types of black shale have different phase peak frequencies and chargeability levels in future

investigations. If so, SIP field surveys would be able to discriminate between the different types of black shale.

The SIP measurements show two peaks in the phase spectra, while the Cole-Cole model should in theory have a single peak. Therefore, a multiple Cole-Cole model should be involved (Vanhala, 1997). The highest frequencies (100 Hz to 100 KHz) of the SIP spectrum, which overlap with SkyTEM low moment bandwidth, show a rather small phase lag (< 4°, Figure 3 b). The phase lag is the largest, 2.6° and 3.8°, for E2 and E3 samples (the two samples that contain the most sulphides) at 117 Hz which corresponds to the latest SkyTEM gates. This could explain why the chargeability distribution inverted from the AEM dataset shows a strong correlation with the presence of Alum shale in the tunnel (Figures 4 b and 12 b). The chargeability level estimated from the relative drop of SIP resistivity over the SkyTEM bandwidth range between 52 mV/V and 126 mV/V for the three samples (Figure 3 a). This is in agreement with the chargeability values inverted from the AEM dataset (Figure 12 b).

Although we observe a correlation across the three types of measurements, more research is needed to investigate the IP spectra in natural soils and the relationships between laboratory results and the inverted spectral parameters measured in the field, both from ground IP (Johansson *et al.*, 2015) and from Airborne EM.

Conclusions

Electrical resistivity investigations at an early phase of a tunnel project can minimize the number of drillings and decrease the geological uncertainty. The two resistivity datasets (ground-based and airborne investigations) show that i) AEM provides high enough resolution for tunnel investigations, ii) ERT is useful for small-scale evaluation but it is limited in depth of investigation. AEM possesses the advantage of large depth of investigation while covering large areas in a relatively short time without requiring access to the ground. In

addition, it is particularly sensitive to conductive anomalies. AEM is however limited in densely populated areas (for safety reasons) and in the presence of infrastructure (for data quality reasons). Its high mobilisation cost limits its application to medium and large geotechnical projects but combining several nearby surveys can be an economical option. The heavily folded shale along our study area illustrates the superior lateral resolution of ERT versus AEM, while both methods are consistent in terms of resolving the vertical boundary of the resistor/conductor interface.

The laboratory results suggest that the amplitude of the SIP phase peak might be a good proxy for the toxicity level of the Alum shale. Chargeability investigations obtained from ground-based methods have a strong potential for black shale mapping. However, the standard and efficient ground-based time-domain acquisition method reveals some limitation due to the high noise level in the voltage data when acquired in a conductive environment. The preliminary results presented on the chargeability derived from AEM method are also promising for contributing to the mapping of these shales. Even at a noisy site, the airborne time-domain IP data present a good correlation with the presence of Alum shale. More research is needed on the induced polarization in black shale to bridge the gap between small-scale laboratory measurements and the inverted parameters in field, both ground and airborne.

Airborne gamma radiation, in particular uranium distribution, is also very sensitive to the presence of Alum shale, but it can be attenuated by clayey overburdens. Fortunately, the data quality does not deteriorate with the presence of infrastructures, as it does for AEM. The two methods are therefore complementary.

Acknowledgements

We thank the Norwegian Public Road authority (SVV) for financing this study and giving permission to publish. We are grateful to Stian Ellingsen and Tore Thomassen (SVV) for permission to publish the geological data used in this study. Valuable comments on Alum shale have been provided by E. Endre (formerly NGI). We express gratitude to Flemming Effersø (SkyTEM Surveys Aps) for effective survey planning as well as Århus University for continuous support and early access to their latest inversion development. We further thank the editor and the three anonymous reviewers for providing thoughtful comments to this manuscript. Funding was also provided by the Research Council of Norway through NGI research programs.

References

ABEM 2010. Terrameter LS Instruction Manual. http://abem.se, pp 63.

AGI 1972. Glossary of Geology American Geological Institute, pp 805.

Anschütz, H., Bazin, S., Kåsin, K., Pfaffhuber, A.A. and Smaavik, T. in review. Airborne sensitive clay mapping - stretching the limits of AEM resolution and accuracy. *Near surface Geophysics.*

Anschütz, H., Vöge, M., Lysdahl, A., Bazin, S., Sauvin, G., Pfaffhuber, A.A. and Berggren, A.L. 2017. From manual to automatic AEM bedrock mapping. Special issue Airborne Geophysics of *J. of Environmental* and *Engineering Geophysics,* **22**, 35-49*. DOI: 10.2113/JEEG22.1.35*

Auken, E., Christiansen, A.V., Jacobsen, B.H., Foged, N. and Sørensen, K.I. 2005. Piecewise 1D laterally constrained inversion of resistivity data. *Geophysical Prospecting*, **53**, 497-506.

Auken, E., Christiansen, A.V., Kirkegaard, C., Fiandaca, G., Schamper, C., Behroozmand, A.A., Binley, A., Nielsen, E., Effersø, F., Christensen, N.B., Sørensen, K. I., Foged, N. and Vignoli, G. 2014. An overview of a highly versatile forward and stable inverse algorithm for airborne, ground-based and borehole electromagnetic and electric data. *Exploration Geophysics.* http://dx.doi.org/10.1071/EG13097

Auken, E., Christiansen, A. V., Westergaard, J. H., Kirkegaard, C., Fopged, N., Viezzoli, A. 2009, An integrated processing scheme for high-resolution airborne electromagnetic surveys, the SkyTEM system. *Exploration Geophysics*, **40**, 184-192.

Bazin, S., Anschütz, H., Lysdahl, A.K., Pfaffhuber, A.A. and Scheibz J. 2015. ERT inversion industry standard versus cutting edge developments, time for a change? *SAGEEP,* Austin, USA.

Dahlin, T. 2000. Short note on electrode charge-up effects in DC resistivity data acquisition using multi electrode arrays. *Geophys. Prospect.,* **48** (1), 181–187.

Christiansen, A. V. and Auken, E. 2012. A global measure for depth of investigation. *Geophysics*, **77**, 171-178.

Dahlin, T. and Leroux, V. 2012. Improvement in time-domain induced polarisation data quality with multi-electrode systems by separating current and potential cables. *Near Surface Geophysics*, **10**, 545-565.

Dahlin, T., and Zhou, B. 2006. Gradient array measurements for multi-channel 2D resistivity imaging. *Near Surface Geophysics,* **4**, 113-123.

Dahlin, T., and Loke, M.H. 2015. Negative apparent chargeability in time-domain induced polarisation data. *Journal of Applied Geophysics*, 1**23**, 322-332.

Danielsen, B.E. and Dahlin, T. 2009. Comparison of geoelectrical imaging and tunnel documentation at the Hallandsås Tunnel, Sweden. *Engineering Geology*, doi:10.1016/j.enggeo.2009.05.005

Fiandaca, G., Ramm, J., Binley, A., Gazoty, A., Christiansen, A. V. and Auken, E. 2013. Resolving spectral information from time domain induced polarization data through 2-D inversion. *Geophysical Journal International*, **192**, 631-646, doi:10.1093/gji/ggs060

Günther, T., Rücker, C., and Spitzer, K. 2006. 3D modelling and inversion of dc resistivity data incorporating topography – II. Inversion. *Geophysical Journal International,* **166**, 506-517.

Günther, T. and Martin, T. 2016. Spectral two-dimensional inversion of frequency-domain induced polarization data from a mining slag heap. *J. of Applied Geophysics*, http://dx.doi.org/10.1016/j.jappgeo.2016.01.008

Heincke, B.H., Smethurst, M.A., Bjørlykke, A., Dahlgren, S., Rønning, J.S. and Mogaard, J.O. 2008. Airborne gamma-ray spectrometer mapping for relating indoor radon concentrations to geological parameters in the Fen region, southeast Norway. *Geology for Society, Geological Survey of Norway*, **11**, 131–143.

Johansson, S., Fiandaca, G. and Dahlin, T. 2015. Influence of non-aqueous phase liquid configuration on induced polarization parameters: Conceptual models applied to a time-domain field case study. *J. of Applied Geophysics,* http://dx.doi.org/10.1016/j.jappgeo.2015.08.010

Kaminsky, V. and Viezzoli, A. 2017. Modeling induced polarization effects in helicopter time-domain electromagnetic data: Field case studies. *Geophysics*, **82**, 49-61, doi:10.1190/geo2016-0103.1

Kratzer, T. and Macnae, J.C. 2012. Induced polarization in airborne EM. *Geophysics*, **77**, E317-E327.

Lysdahl, A. K., Bazin, S., Anschütz, H. and Pfaffhuber, A.A. 2015. Black shale mapping by AEM for geotechnical applications. EAGE *European Airborne Electromagnetics Conference*, Turin, Italy.

Lysdahl, A. K., Endre, E. and Radic, T. 2016. The IP response of black shales in the Oslo graben, Norway. *5th international workshop on Induced Polarization*, in Århus, Danmark.

Loke, M.H. 2010. RES2DINV version 3.59.102. Geoelectrical Imaging 2D and 3D. Instruction Manual. *Geotomo Software*, http://www.geotomosoft.com

NGI 2013. Tunnel Gran Jaren: identifisering og karakterisering av skiferhorisonter i tunneltrasé. *NGI report* 20120110-01R, pp 43.

NGI 2015. Identifisering og karakterisering av syredannende bergarter. *NGI report* 20120842-01R, pp57. Public document in Norwegian for the Norwegian Environment Agency. http://www.miljodirektoratet.no/Documents/publikasjoner/M310/M310.pdf

NGU, 2009. A compilation of previously published geochemical data on the lower Cambro-Silurian sedimentary sequence, including the alum shales in the Oslo region. *NGU report* 2009.053, pp25.

Nielsen, A.T. and Schovsbo, N.H. 2007. Cambrian to basal Ordovician lithostratigraphy in southern Scandinavia. *Bulletin of the Geological Society of Denmark*, **53**, 82–84.

Nyland, B. and Teigland, J. 1984. Sedimentologisk og geokjemisk undersøkelse av de kambriske og underordoviciske marine sedimenter i Oslofeltet. *Thesis*. Geologisk institutt, Universitetet i Oslo, pp196.

Oldenburg, D. W. and Li, Y. 1994. Inversion of induced polarization data. *Geophysics*, **59**, 1327–1341.

Olsson, P.-I., Dahlin, T., Fiandaca, G. and Auken, E. 2015. Measuring time-domain spectral induced polarization in the on-time: decreasing acquisition time and increasing signal-to-noise ratio. *J. of Applied Geophysics*, http://dx.doi.org/10.1016/j.jappgeo.2015.08.009

Okazaki, K., Mogi, T., Utsugi, M., Ito, Y., Kunishima, H., Yamazaki, T., Takahashi, Y., Hashimoto, T., Ymamaya, Y., Ito, H., Kaieda, H., Tsukuda, K., Yuuki, Y. and Jomori, A. 2011. Airborne electromagnetic and magnetic surveys for long tunnel construction design. *Phys. Chem. Earth*, **36**, 1237–1246.

Pelton, W. H., Ward, S. H., Hallof, P. G., Sill, W. R. and Nelson P. H. 1978. Mineral discrimination and removal of inductive coupling with multifrequency IP. *Geophysics*, 43, 588–609, doi: 10.1190/1.1440839

Pfaffhuber, A. A., Grimstad, E., Domaas, U., Auken, E., Halkjær, M., and Foged, N. 2010. Airborne EM Mapping of Rock Slides and Tunneling Hazards, EAGE *16th European Meeting of Environmental and Engineering Geophysics*, Zurich, Switzerland, B10.

Radic, T. 2014. Measuring IP effects at high frequencies: First lab and field data from 0.001 Hz – 250 kHz*. 3rd international workshop on Induced Polarization*, Boulder Colorado, USA.

Revil, A., Mao, D., Shao, Z., Sleevi, M. F. and Wang, D. 2016. Induced polarization response of porous media with metallic particles — Part 6: The case of metals and semimetals. *Geophysics*, **82**, doi: 10.1190/geo2016- 0388.1

Smith, R.S. and Klein, J. 1999. A special circumstance of airborne induced polarization measurements. *Geophysics*, **61**, 6-73.

Smith, R.S. and West, G.F. 1989, Field examples of negative coincident-loop transient electromagnetic responses modeled with polarizable half-planes. *Geophysics*, **54**, 1491-1498.

Sørensen, K.I. and Auken, E. 2004. SkyTEM – A new high-resolution helicopter transient electromagnetic system. *Exploration Geophysics,* **35**, 191-199.

Vanhala, H., 1997. Laboratory and field studies of environmental and exploration applications of the spectral induced-polarization (SIP) method. *PhD thesis*, Geologian Tutkimuskeskus, Helsinki University of Technology,Espoo, Finland.

Viezzoli, A., Christiansen, A.V., Auken, E. and Sørensen, K.I. 2008. Quasi-3D – modeling of airborne TEM data by Spatially Constrained Inversion. *Geophysics,* **73**, F105-F113.

Viezzoli, A., Jørgensen, F and Sørensen, C. 2012. Flawed Processing of Airborne EM Data Affecting Hydrogeological Interpretation. *Groundwater,* **51** (2), 191-202.

Viezzoli, A., and Kaminski, V. 2016. Airborne IP: examples from the Mount Milligan deposit, Canada, and the Amakinskaya kimberlite pipe, Russia. Exploration Geophysics, http://dx.doi.org/10.1071/EG16015.

Wang, Z., Gelius, L.J. and Kong, F.N., 2009. Simultaneous core sample measurements of elastic properties and resistivity at reservoir conditions employing a modified triaxial cell - A feasibility study. *Geophysical Prospecting*, **576**, 1009–1026.

Wennermark, M., Olsson, P.-I., Johansson, S. and Hellman, K. 2015. A Comparison of DCIP Inversion Software. EAGE *European Airborne Electromagnetics Conference*, Turin, Italy.

List of tables

List of figures

Figure 1: Detailed map of the study area in Gran town, 100 km north of Oslo, Norway. Superposition of the planned road tunnel, the ERT profiles, the AEM test survey and the bedrock stratigraphy. The regional map is displayed with transparency effect to show the presence of urban infrastructure near the survey.

Figure 2: Left: the modified triaxial cell can measure resistivity at in-situ conditions (Wang *et al*., 2009). The electrodes are encapsulated in the top cap and the pedestal and on the sides of the sample. Right: Alum shale sample used for the laboratory resistivity measurement. Notice the anisotropy and the large mineral sizes.

Figure 3: Complex resistivity spectra ($\rho^* = |\rho| e^{i\varphi}$) on three core samples E1, E2 and E3 of Alum shale. The resistivity amplitude $|\rho|$ is shown in *a*, while the phase φ shift (in degrees) between the injected current and the measured potential is shown in *b*.

Figure 4: a: resistivity models along G1, G4 and G3. b: preliminary geology model based on drilling (background colours) and geological mapping during excavation (inside tunnel sketch). The vertical scale is exaggerated.

Figure 5: Pseudo-sections along G3 showing good quality apparent resistivity data (upper panel) and noisy IP data (three lower panels). The first gate, IP1, extends from 0.01 to 0.03 s. The last gate, IP9, extends from 0.75 to 0.99 s. The normalized apparent chargeability data is the integration over the 9 time gates. The triangle pointing downwards indicates the position of the measurement shown in Figure 6 for which the chargeability data is of good quality. The triangle pointing upwards indicates the position of the measurement shown in Figure 7 for which the chargeability data is of bad quality.

Figure 6: Voltage measurements (upper) and resulting decay curve (lower) collected along G3 at the location marked by triangle pointing downwards in Figure 5.The voltage data is of good quality and so is the resulting decay curve.

Figure 7: Voltage measurement (upper) and resulting decay curve (lower) collected at the location along G3 marked by a triangle pointing upwards in Figure 5. The voltage data is influenced by noise.

Figure 8: Resistivity (*a* and *c*) and chargeability (*b* and *d*) models along G1. Res2Dinv models are seen in *a* and *b* while BERT models are seen in *c* and *d*. The resistivity data is of good quality while the IP data is strongly influenced by noise.

Figure 9: Resistivity (*a* and *c*) and chargeability (*b* and *d*) models along G4. Res2Dinv models are seen in *a* and *b* while BERT models are seen in *c* and *d*. The resistivity data is of good quality while the IP data is strongly influence by noise.

Figure 10: Resistivity (a and c) and chargeability (b and d) models along G3. Res2Dinv models are seen in a and b while BERT models are seen in c and d. The raw data is shown in Figure 5: the resistivity data is of good quality while the IP data is strongly influenced by noise.

Figure 11: a) AEM raw and stacked voltage soundings at low moment (LM) and high moment (HM) measured over 2 minutes of flight. The manually edited soundings are shown in grey. The area marked in red shows noisy data affected by capacitive coupling due to man-made infrastructures. b) Transient of LM and HM as a result of the averaged data marked in blue in a).

Figure 12: AEM derived resistivity (a) and chargeability m_o (b) vertical sections projected along the Gran tunnel, obtained with the SCI of a dispersive resistivity model (Cole - Cole). Cf. Figure 3 for the coincident geological section. The resistivity colours scale and the horizontal distances are the same as in Figure 4.

Figure 13: Maps showing the AEM derived resistivity models near Gran tunnel during the test survey (point themes) compared to the radiometry data (solid map, only the uranium distribution is shown). The average resistivity maps are taken at three different elevation slices intersected by the tunnel.

Figures

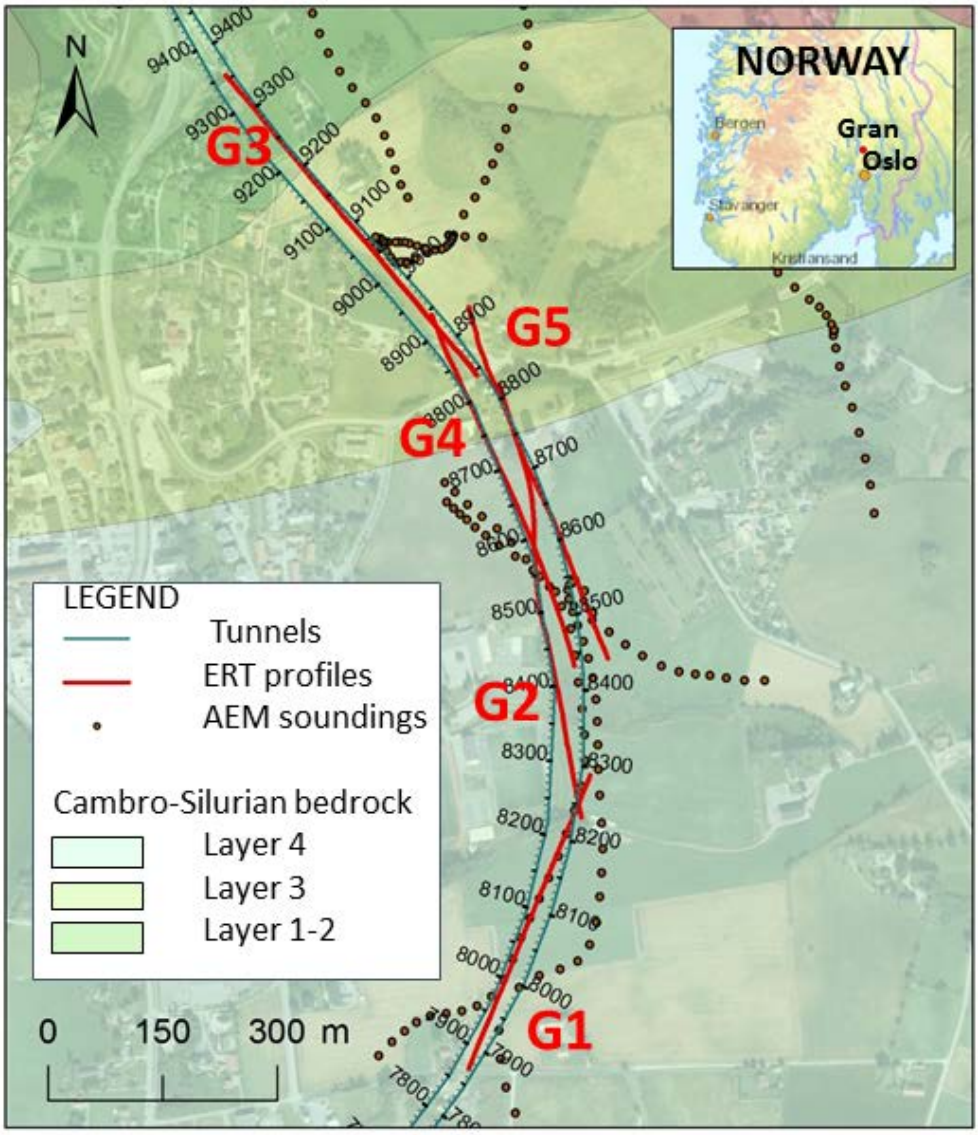

Figure 1: Detailed map of the study area in Gran town, 100 km north of Oslo, Norway. Superposition of the planned road tunnel, the ERT profiles, the AEM test survey and the bedrock stratigraphy. The regional map is displayed with transparency effect to show the presence of urban infrastructure near the survey.

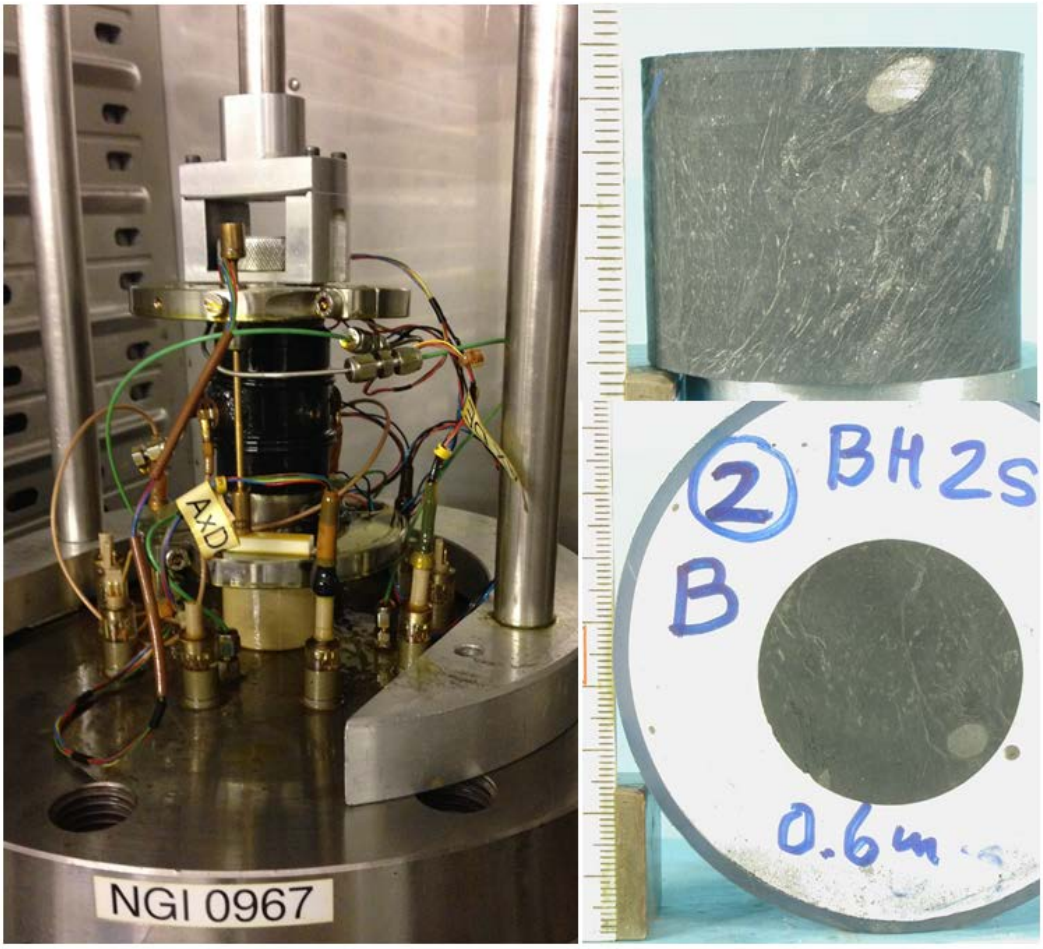

Figure 2: Left: the modified triaxial cell can measure resistivity at in-situ conditions (Wang et al., 2009). The electrodes are encapsulated in the top cap and the pedestal and on the sides of the sample. Right: Alum shale sample used for the laboratory resistivity measurement. Notice the anisotropy and the large mineral sizes.

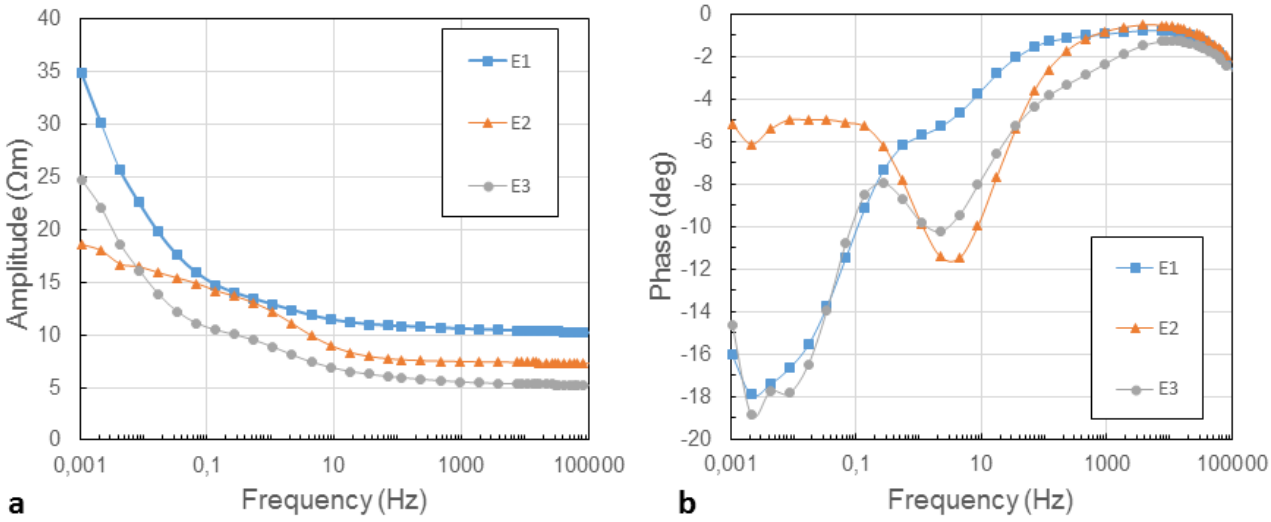

Figure 3: Complex resistivity spectra (ρ* = |ρ| eiφ) on three core samples E1, E2 and E3 of Alum shale. The resistivity amplitude |ρ| is shown in *a*, while the phase φ shift (in degrees) between the injected current and the measured potential is shown in *b.*

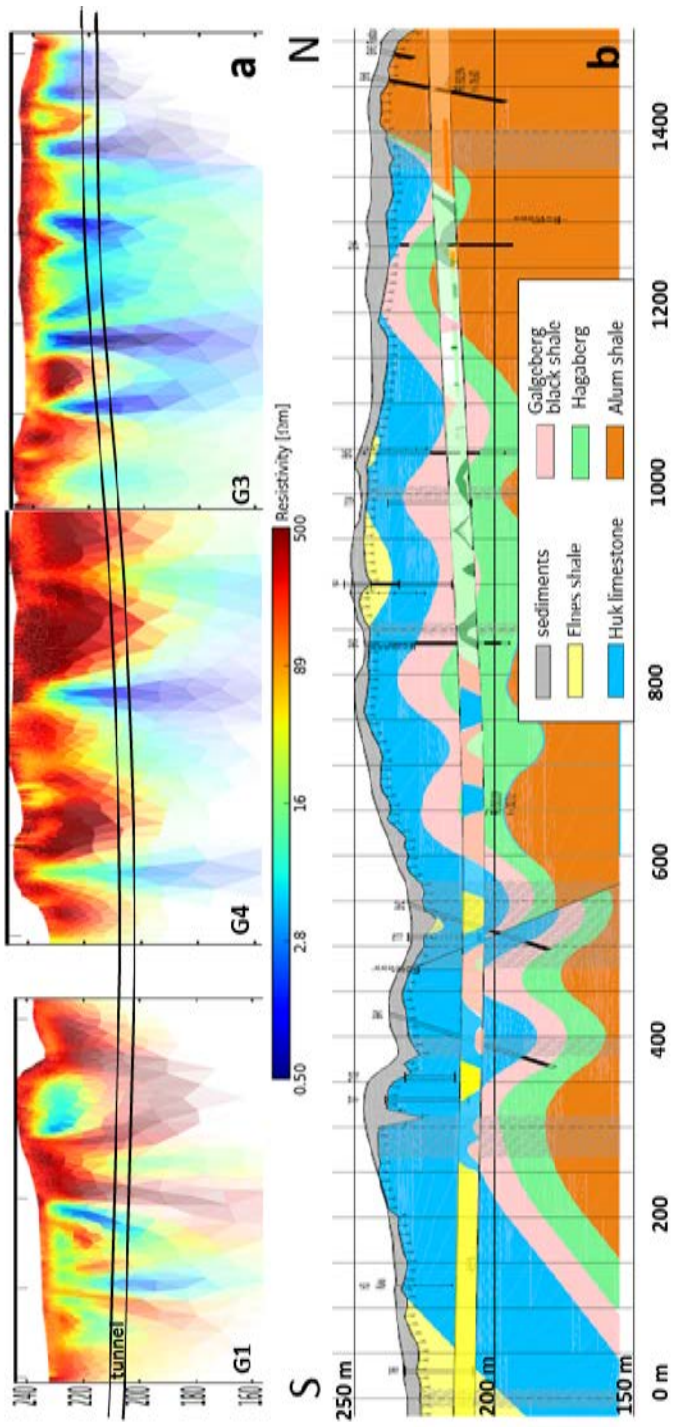

Figure 4: a: resistivity models along G1, G4 and G3. b: preliminary geology model based on drilling (background colours) and geological mapping during excavation (inside tunnel sketch). The vertical scale is exaggerated.

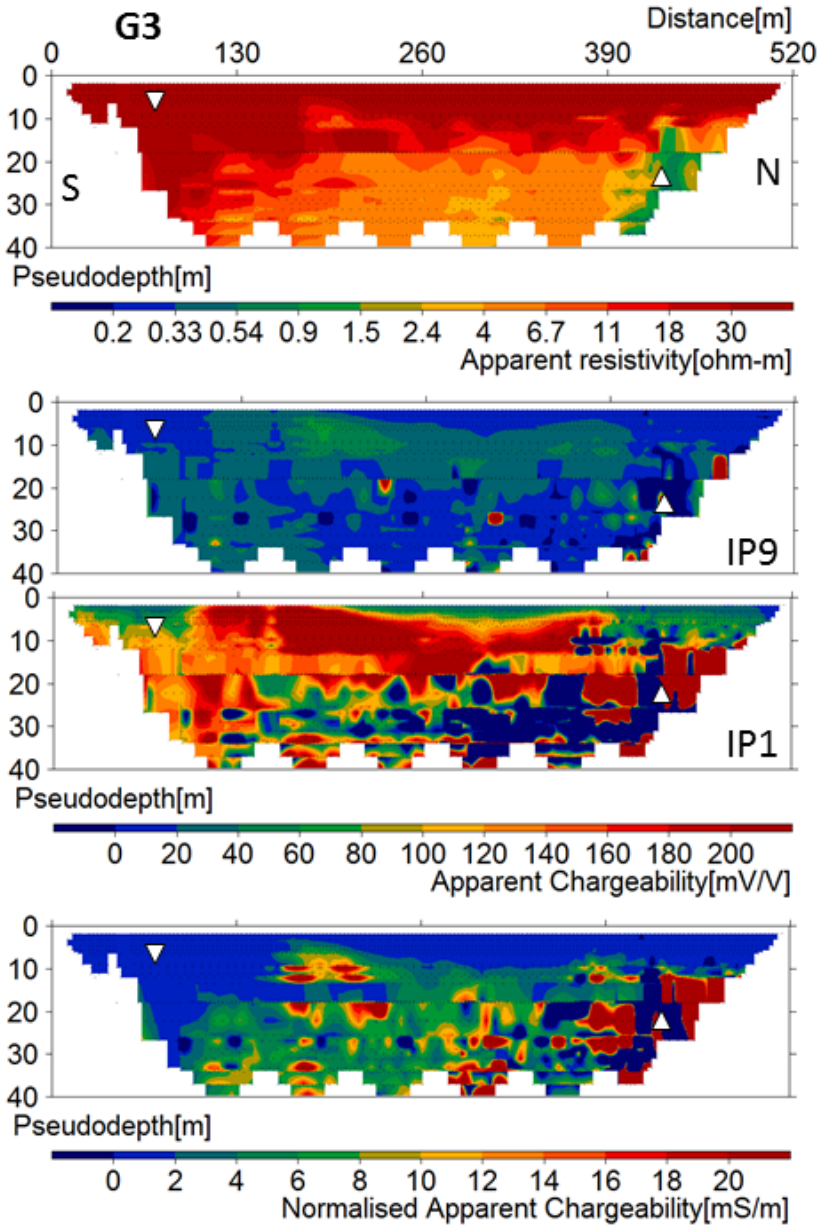

Figure 5: Pseudo-sections along G3 showing good quality apparent resistivity data (upper panel) and noisy IP data (three lower panels). The first gate, IP1, extends from 0.01 to 0.03 s. The last gate, IP9, extends from 0.75 to 0.99 s. The normalized apparent chargeability data is the integration over the 9 time gates. The triangle pointing downwards indicates the position of the measurement shown in Figure 6 for which the chargeability data is of good quality. The triangle pointing upwards indicates the position of the measurement shown in Figure 7 for which the chargeability data is of bad quality.

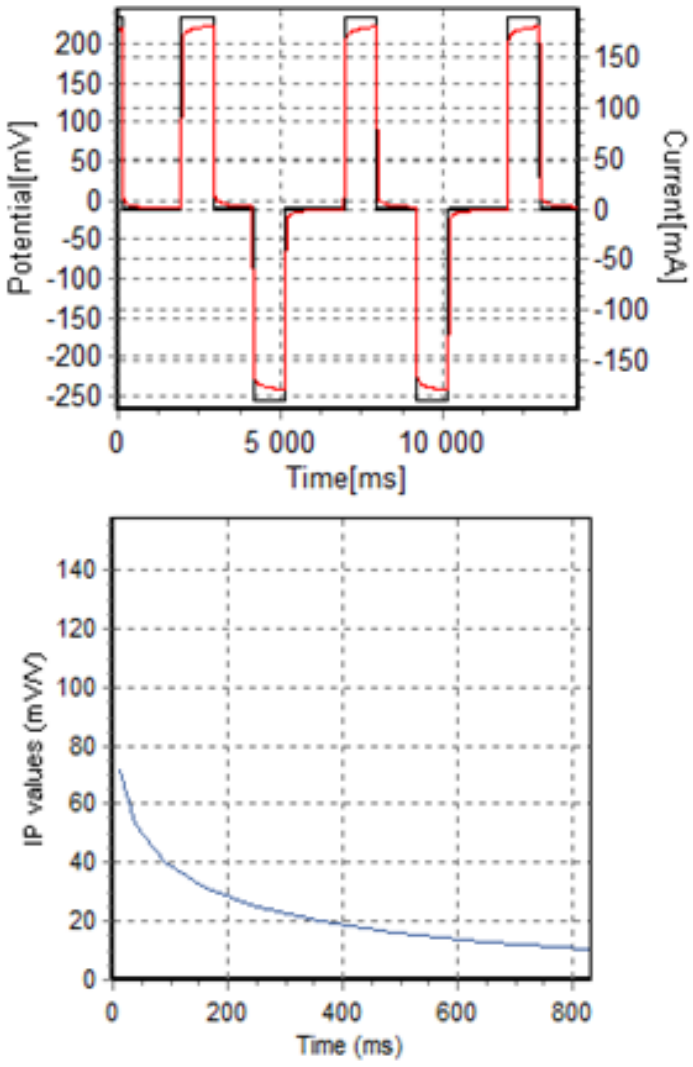

Figure 6: Voltage measurements (upper) and resulting decay curve (lower) collected along G3 at the location marked by triangle pointing downwards in Figure 5.The voltage data is of good quality and so is the resulting decay curve.

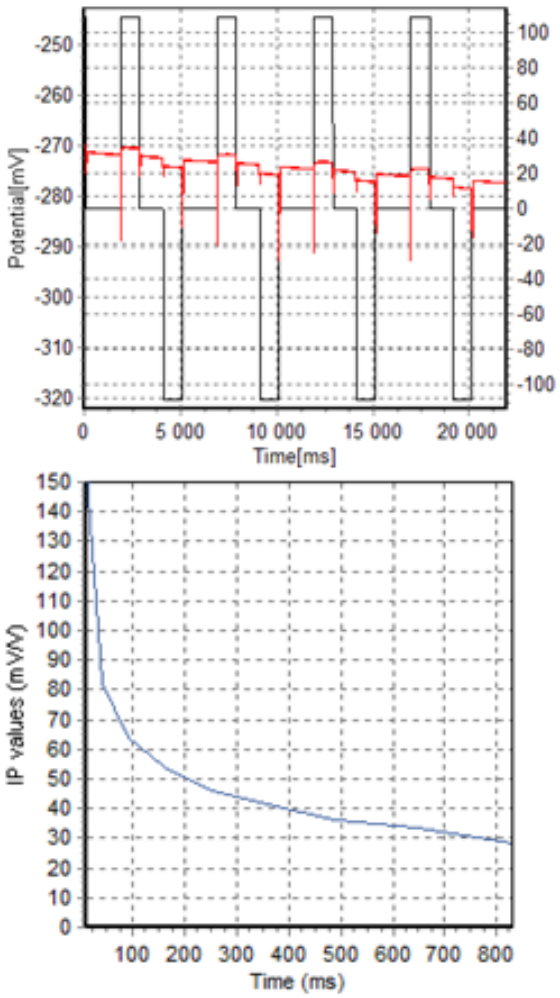

Figure 7: Voltage measurement (upper) and resulting decay curve (lower) collected at the location along G3 marked by a triangle pointing upwards in Figure 5. The voltage data is influenced by noise.

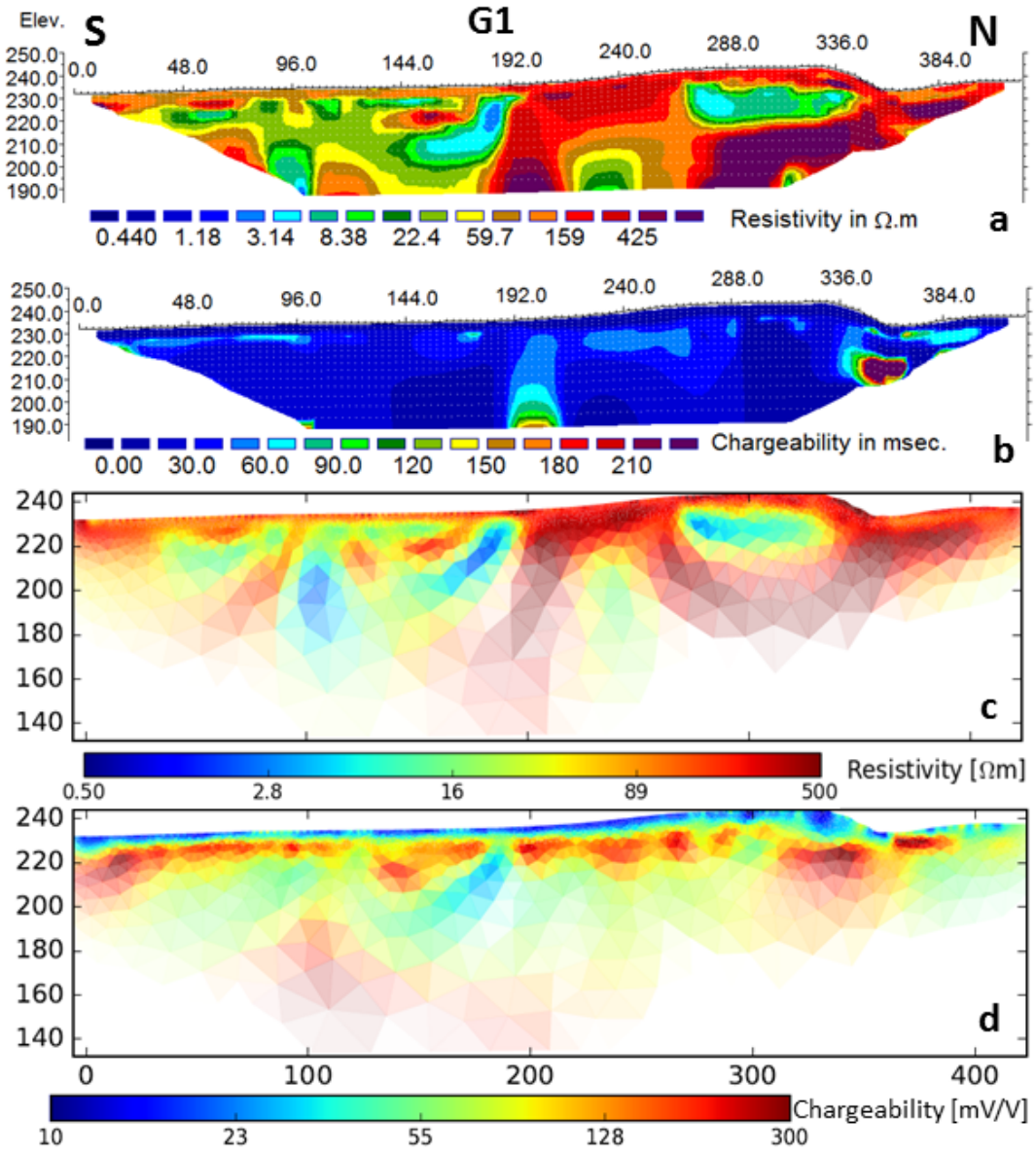

Figure 8: Resistivity (a and c) and chargeability (b and d) models along G1. Res2Dinv models are seen in a and b while BERT models are seen in c and d. The resistivity data is of good quality while the IP data is strongly influenced by noise.

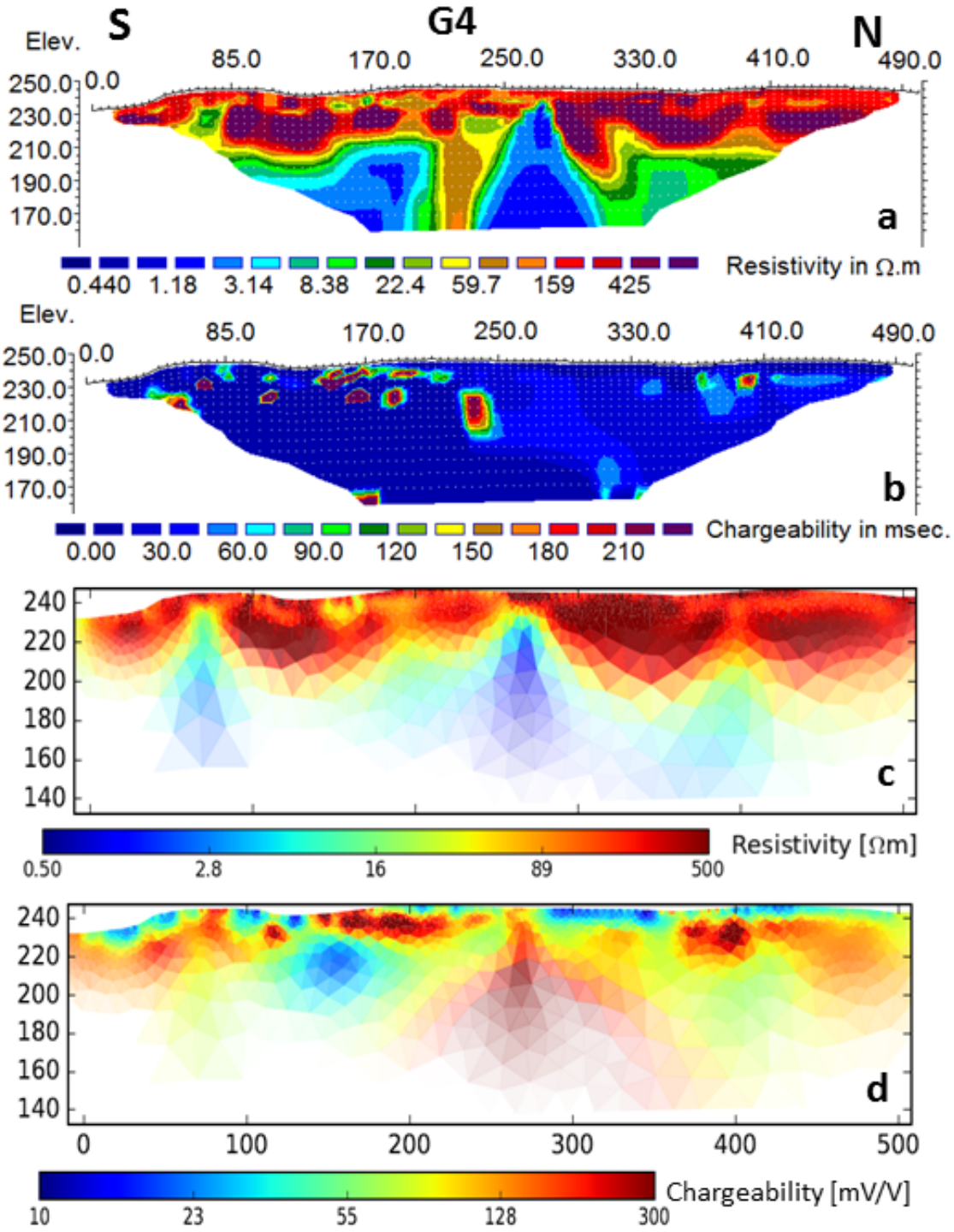

Figure 9: Resistivity (a and c) and chargeability (b and d) models along G4. Res2Dinv models are seen in a and b while BERT models are seen in c and d. The resistivity data is of good quality while the IP data is strongly influence by noise.

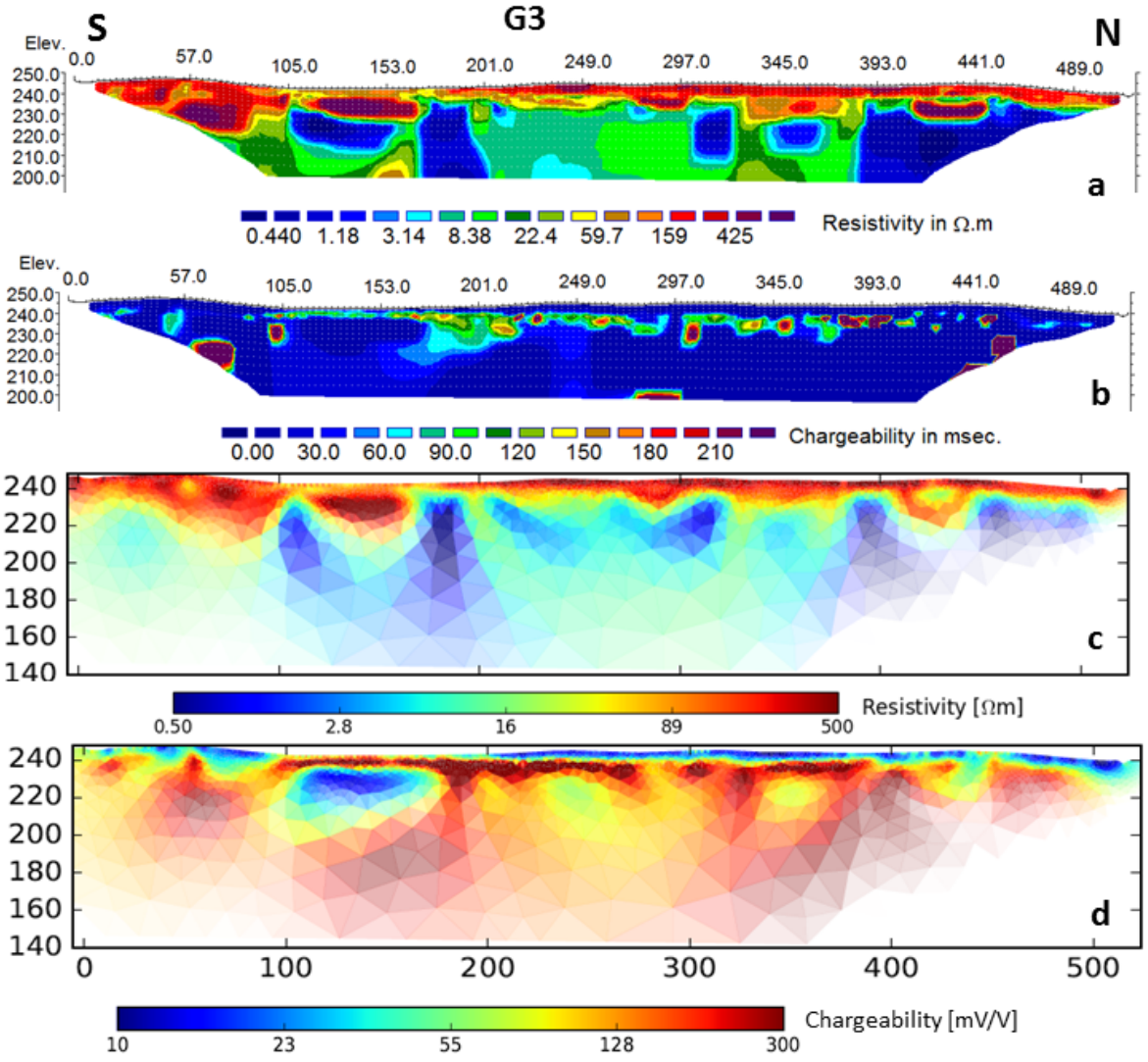

Figure 10: Resistivity (a and c) and chargeability (b and d) models along G3. Res2Dinv models are seen in a and b while BERT models are seen in c and d. The raw data is shown in Figure 5: the resistivity data is of good quality while the IP data is strongly influenced by noise.

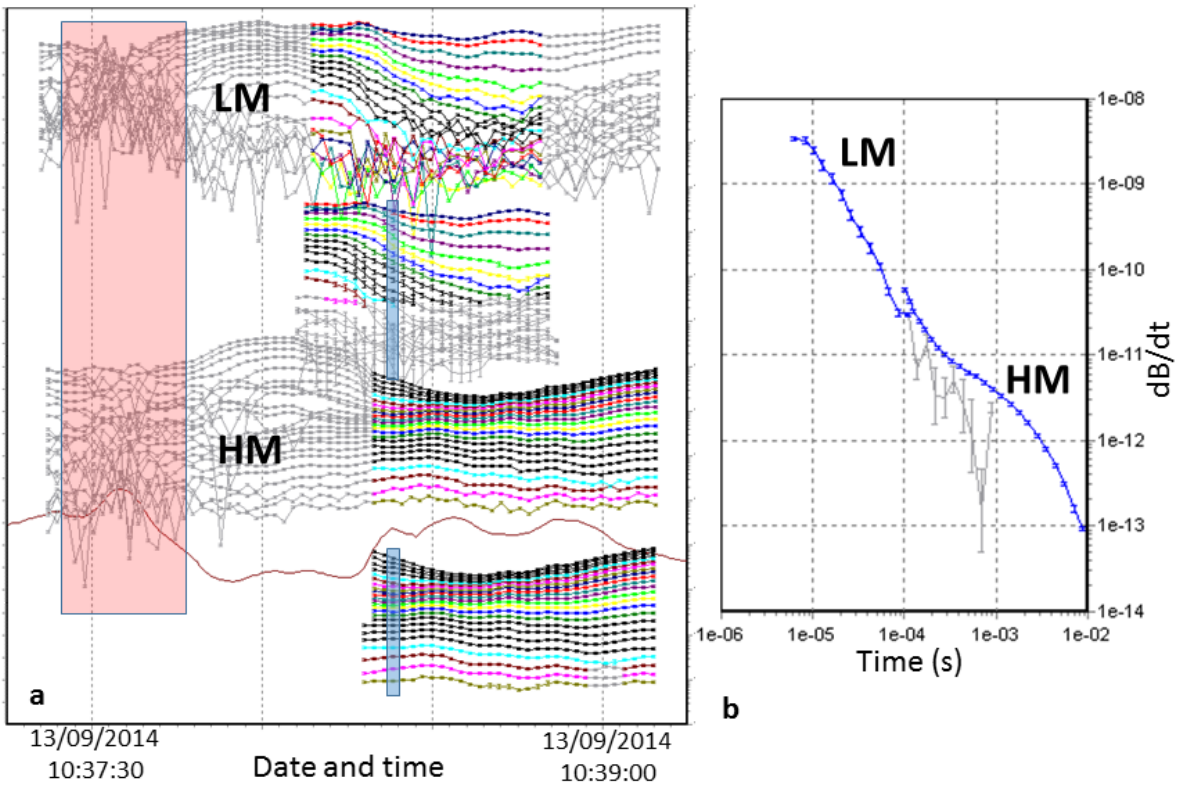

Figure 11*: a) AEM raw and stacked voltage soundings at low moment (LM) and high moment (HM) measured over 2 minutes of flight. The manually edited soundings are shown in grey. The area marked in red shows noisy data affected by capacitive coupling due to man-made infrastructures. b) Transients of LM and HM as a result of the averaged data marked in blue in a).*

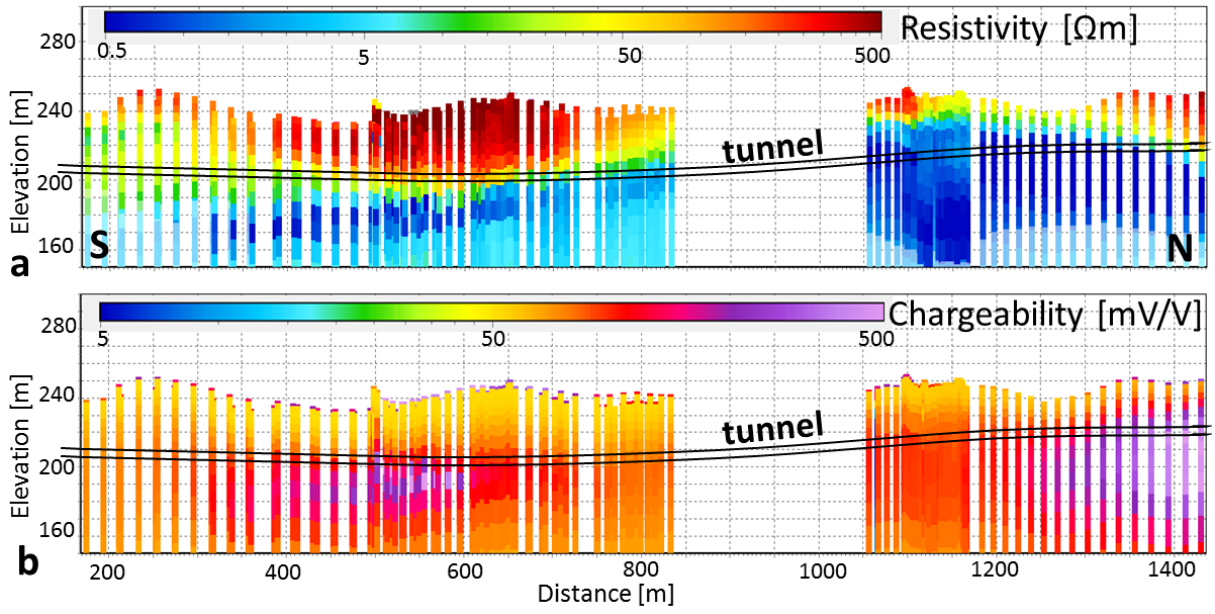

Figure 12*: AEM derived resistivity (a) and chargeability m_o (b) vertical sections projected along the Gran tunnel, obtained with the SCI of a dispersive resistivity model (Cole - Cole). Cf. Figure 3 for the coincident geological section. The resistivity colours scale and the horizontal distances are same as in Figure 4.*

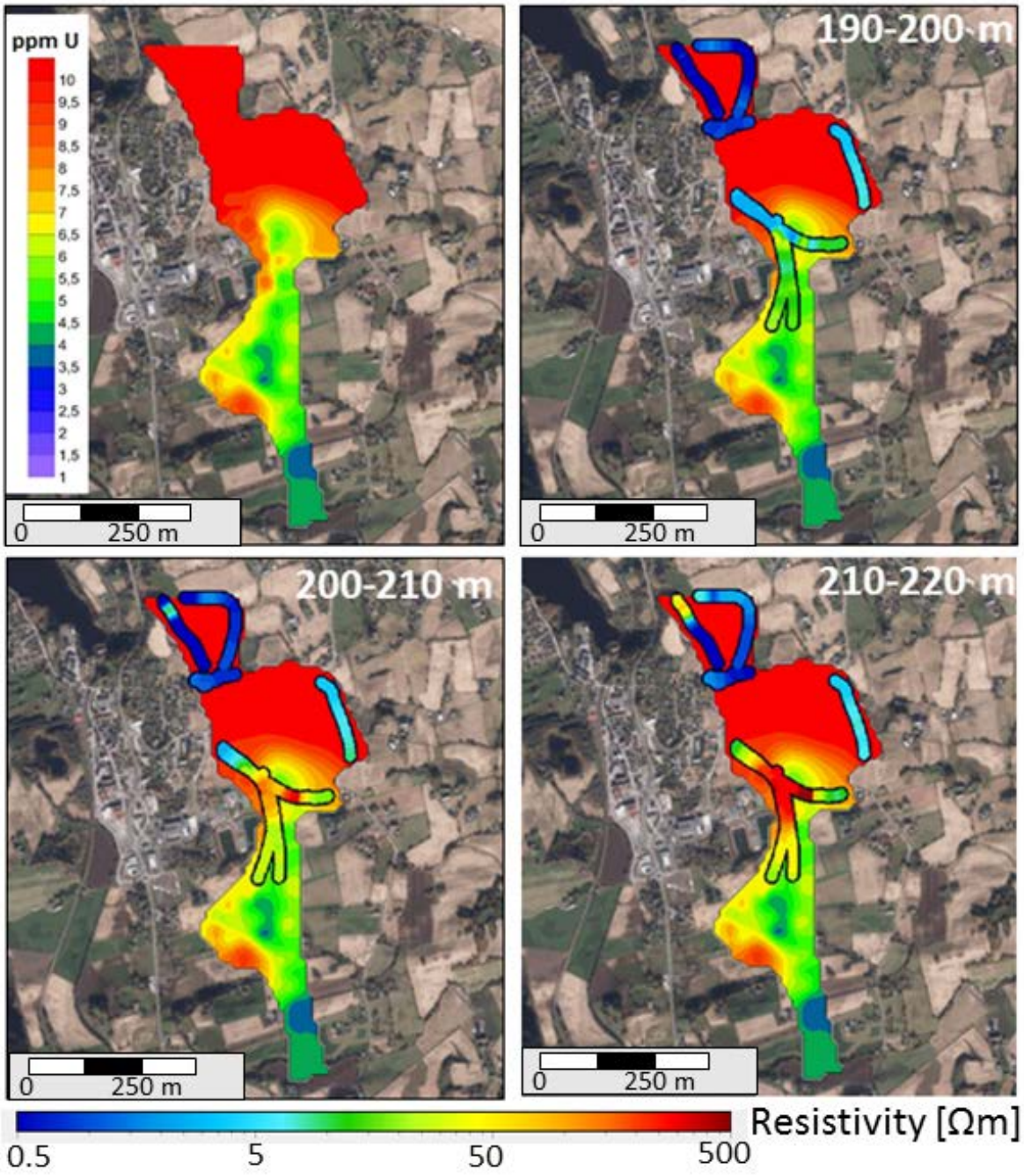

Figure 13: Maps showing the AEM derived resistivity models near Gran tunnel during the test survey (point themes) compared to the radiometry data (solid map, only the uranium distribution is shown). The average resistivity maps are taken at three different elevation slices intersected by the tunnel.